

Guided wave tomography based on least-squares reverse-time migration

Structural Health Monitoring

2020, Vol. 19(4) 1237–1249

© The Author(s) 2019

Article reuse guidelines:

sagepub.com/journals-permissions

DOI: 10.1177/1475921719880296

journals.sagepub.com/home/shm

Jiaze He¹ , Daniel C Rocha² and Paul Sava²

Abstract

A key to successful damage diagnostics and quantification is damage imaging through ultrasonic guided wave tomography. We propose the implementation of least-squares reverse-time migration in a circular array for damage imaging in an aluminum plate. The theory of least-squares reverse-time migration is formulated for guided wave applications along with the summary of an efficient optimization algorithm: the conjugate gradient method. Numerical simulation and laboratory experiments are used to evaluate its performance with a circular array setup. In order to improve the data processing efficiency, the concept of using a limited number of actuators but a relatively large number of sensors is tested. Studies are conducted on three numerical cases, including a rectangular-shaped damage site, a complex-shaped damage site, and six other damage sites varying in size. As an inversion-based method, least-squares reverse-time migration shows significantly improved shape reconstruction with the amplitude quantification capability, compared to conventional reverse-time migration. Our experimental data are generated by piezoelectric wafers as actuators, measured by a scanning laser Doppler vibrometer to form a circular array on an aluminum plate, with a rectangular notch located in the inner region of the array. The damage images using experimental data show consistency in both the simulations using Born scattering and in altered material properties in the damaged region. According to the comparison, least-squares reverse-time migration for guided wave tomography is a promising technology to provide high-resolution large area damage imaging for plate-like structures.

Keywords

Least squares, reverse-time migration, guided waves, damage imaging, inversion

Introduction

Damage diagnostics is the central pillar in both structural health monitoring (SHM)¹ and nondestructive evaluation (NDE).² As a rapid damage diagnostic technique, ultrasonic guided waves receive increasing attention due to their superior characteristics in long-distance propagation, large area coverage, and through-thickness inspection capability.³ Signals measured by various types of ultrasonic sensors can be converted to diagnostic results.^{4–9}

One category of ultrasonic damage diagnostic methods directly creates the results as damage indices or images. A damage index can be defined in various manners^{10,11} for monitoring a path between a pair of sensors. Damage indices are convenient to use, but the results are usually some scalar values¹² or rather coarse images.¹³ For quantitative SHM and NDE, damage images meeting certain resolution requirements are preferred. Total focusing method (TFM) is a popular bulk

wave imaging algorithm, where each received signal contributes to the final imaging through the delay-and-sum (DAS) process.¹⁴ This process can also be implemented in the frequency wavenumber domain¹⁵ and accounts for multiple modes.¹⁶ DAS and its variations are also applied in guided wave imaging. They can be implemented using both a sparse array¹⁷ and a phased array.^{18,19} Another imaging algorithm, time-reversal-based multiple signal classification, achieves resolution finer than half of the input wavelength.^{20,21}

¹Department of Aerospace Engineering and Mechanics, The University of Alabama, Tuscaloosa, AL, USA

²Center for Wave Phenomena, Colorado School of Mines, Golden, CO, USA

Corresponding author:

Jiaze He, Department of Aerospace Engineering and Mechanics, The University of Alabama, Tuscaloosa, AL 35487, USA.

Email: jhe26@eng.ua.edu

Although the above direct approaches aim for damage index generation or imaging, the results are not used to generate quantitative comparisons with the measured signals. In contrast, when a damage diagnostic or imaging technique “requires the use of a model and the identification of the parameters of this model,”²² it falls into the category of inverse methods. Because the damage diagnostic or imaging process includes further fitting the synthetics generated by a model with experimental measurements, the results from those non-trivial inverse methods are often considerably better than the above direct methods.²³ Thus, solving inverse problems properly is essential in damage diagnostics.

Various inverse problems in SHM or NDE face different levels of difficulties. Depending on the parameterization of a damage model, the resultant parameters differ significantly by the orders of dimensions. For determining the existence of any damage, the possible parameter is simply binary; for damage localization, the dimensions of the parameter space equal the number of possible locations, for each damage site. In most of the inverse problems, the large number of unknowns is much more than the measured data in dimensions. As a result, the inverse problems are frequently “ill-posed,”²² which means the solution cannot be uniquely determined based on the measured data. Two-stage approach can significantly reduce the dimensions of the inverse problems in both metallic²⁴ and composite structures.²⁵

A relatively low-dimensional inverse problem is to estimate the material properties using ultrasonic measurements.^{26,27} Ultrasonic guided wave suits the task, because its dispersion relation is uniquely determined by the material properties.²⁸ In these problems, material properties are assumed to be constant across the one-dimensional (1D) spatial measurement of guided waves. As a result, the inversion for those material constants only requires the determination of a few parameters. For instance, Young’s modulus, Poisson’s ratio, and the plate thickness were inverted for an adhesive layer in Koreck et al.²⁶ This type of inversion is performed through best estimating these parameters to fit the dispersion relationship and created using experimental measurements.²⁷

Higher dimensions of inverse problems are commonly formulated for damage imaging, in which each pixel is, at least, one parameter to be inverted for. For example, TFM can be modified to an inverse method with much better performance through inverting damage simply as binary values at a variety of locations.²⁹ Leonard et al.³⁰ proposed a straight-ray tomography technique using Lamb waves to reconstruct the averaged group velocity of composite materials. Similarly, the wall thickness profile was reconstructed through

inverting for the maximum corrosion depth and width of a simplified Gaussian-shaped damage model, by minimizing the phase differences in those straight-ray measurements.³¹

Since diffraction effects were not taken into account with straight-ray measurements, this type of tomography is often limited in resolution and inaccurate in damage model reconstruction. To improve the resolution, diffraction tomography (DT) is formulated, utilizing diffracted ultrasonic guided waves, where a damage site is modeled as a perturbation for inversion.^{32–34} Hybrid algorithm for robust breast ultrasound tomography (HARBUT),³⁵ based on theoretical Green’s functions, utilizes the DT as an initial model of a scattering object. Its performance on wall thickness loss estimation was quantified for a setup using a limited-view array in Huthwaite.³⁶

One assumption in DT is that the damage is weakly scattered, which might not always be an accurate assumption in damage diagnostics.³⁷ This leads to inverse scattering problems, which describes damage as a strong scattering potential, similar to the theory formulated in general ultrasonics.^{38,39} As a result, the improvement of an imaging algorithm’s resolution can be expected. In Huthwaite et al.,⁴⁰ for instance, a more complex scattering model using HARBUT was created by adding the directivity of damage scattering of guided waves for resolution improvement.

In recent years, full waveform inversion (FWI) was introduced for guided wave tomography using spatial-frequency inversion of damage velocity model as an acoustic model.⁴¹ Originated in geophysics, FWI using guided waves has been successful in thickness map reconstruction through converting the inverted phase velocity model to the thickness loss.⁴² The inversion-based imaging methods are often more computationally intensive such that efforts are made to reduce computational costs such as building a surrogate forward model⁴³ or adding constraints on the sparsity of the model.^{44,45} However, with the development of hardware in recent years, especially the graphical processing unit (GPU), inverse methods that are computationally intensive become more and more viable.^{46,47}

Among a variety of parameters for damage modeling, the reflection coefficient is one of the most suitable parameters. It clearly depends on the depth or severity of damage.^{48,49} Harvesting the non-dispersive characteristic of shear-horizontal (SH) waves,^{50,51} Wang and Hirose⁵² inverted damage shapes using reflection coefficients of damage-scattered SH waves.

One of the suitable imaging algorithms in guided wave imaging that can estimate the reflective coefficients is reverse-time migration (RTM).^{53,54} RTM is a technique developed for geophysical imaging based on a two-way wave propagator.⁵⁵ This imaging method is

named in such a way because it migrates recorded wave events from receivers to the desired imaged locations by back-propagation in time. It is well suited for use with limited-view aperture arrays and has been introduced to guided wave-based damage imaging with success.^{56,57} He and Yuan⁵³ implemented a two-dimensional (2D) limited-view scan with RTM using a normalized zero-lag cross-correlation (NZLCC) imaging condition for isotropic plates and composite laminates,⁵⁴ in which the resulting images approximate the reflection coefficient (reflectivity) of the damage. Some imaging conditions that can potentially be used in conjunction with guided wave RTM are based on displacement wavefield,⁵⁸ scalar wavefield,⁵⁹ or energy norms.^{60–62}

However, RTM images often contain various undesirable artifacts which hinder the application of RTM using guided waves for real-world NDE and SHM. Those artifacts, for instance, might be caused by limited acquisition coverage and bandwidth, which are problems frequently seen in different guided wave imaging techniques.⁶³ Least-squares migration (LSM) is an improved imaging algorithm that reduces these migration artifacts and also improves the resolution of migrated images. LSM is a linearized waveform inversion that seeks to find the image that best predicts, in a least-squares sense, the recorded seismic data.^{64,65} When LSM uses RTM engine, it is referred to as least-squares reverse-time migration (LSRTM).^{66–68} With all the potential benefits, however, LSRTM has not been implemented in ultrasonic guided wave-based damage imaging.

The main purpose of this research is to study the performance of LSRTM with a full-aperture array setup using ultrasonic guided waves. This research differs from the previous work⁶⁹ by revising the implementation to include multiple actuators, replacing the 2D array with a circular, full-aperture array, studying complex-shaped or multi-sized damage sites, and discussing the capability of scattering amplitude recovery by LSRTM. The proposed non-destructive testing (NDT)/SHM technology aims to provide the capability for damage modeling and tracking in Digital Twin application.⁷⁰ The remainder of this article is organized as follows. First, the principles of RTM are briefly presented. Next, the theory of LSRTM and an efficient optimization method are discussed, in the context of ultrasonic guided waves with multi-actuation implementation. Finally, a series of numerical and experimental results using conventional RTM and LSRTM are presented.

Theoretical formulation of LSRTM

As detailed in He and Yuan⁵³ and He et al.,⁷¹ the conventional RTM contains three steps: the simulation of

the forward wavefield, the back-propagation of the time-reversed received signals, and the application of imaging conditions. With proper imaging conditions,⁵⁴ the damage reflectivity can be obtained in the images. To further improve the imaging quality from RTM and reduce artifacts, the LSRTM is proposed in this research. In this section, we will introduce our work⁶⁹ on extending the LSRTM theory to guided wave applications. The multi-actuator consideration is also added in the following expressions.

In guided wave damage imaging, forward modeling in numerical simulation is numerically generated wavefields excited by actuators, using structural and damage models. In this research, the selected damage model parameter is its scattering amplitude \mathbf{m} , which is defined as the amplitude ratio between the scattered waves and the incident waves. In this article, \mathbf{m} is a 2D spatial map, in which each pixel quantifies scatterer strength. At each pixel location, the source time function of the scattered wavefield is created as the product between the scattering amplitude at this position and the time-vary incident wave signals. The scattering modeled in such a manner is essentially based on Born approximation, and this modeling method will be referred to as “Born modeling.”^{72,73}

Mathematically, the forward modeling process for all actuations can be represented by a formal modeling operator \mathbf{F} as

$$\mathbf{d}_{obs} = \mathbf{F}\mathbf{m}_{true} \quad (1)$$

where \mathbf{d}_{obs} is the received damage-scattered data at the sensor array for all actuations. Then migration is the adjoint of the forward modeling,⁷⁴ which can be expressed as

$$\mathbf{m}_{mig} = \mathbf{F}^T \mathbf{d}_{obs} \quad (2)$$

where \mathbf{F}^T is the adjoint operator that transforms received data \mathbf{d}_{obs} into the image \mathbf{m}_{mig} . Essentially, \mathbf{F}^T includes the stacking of the images from all actuations. The backward wavefield is also referred to as “adjoint wavefield.” From equations (1) and (2), the relationship between the migration image and the true reflectivity image is⁷⁵

$$\mathbf{m}_{mig} = \mathbf{F}^T \mathbf{F} \mathbf{m}_{true} \quad (3)$$

Theoretically, the true reflectivity image \mathbf{m}_{true} can be estimated as

$$\hat{\mathbf{m}}_{true} = (\mathbf{F}^T \mathbf{F})^{-1} \mathbf{m}_{mig} = (\mathbf{F}^T \mathbf{F})^{-1} \mathbf{F}^T \mathbf{d}_{obs} \quad (4)$$

However, in practical applications, the inverse of $\mathbf{F}^T \mathbf{F}$ is usually too expensive to compute.⁶⁶ Instead of directly calculating equation (4) to find the solution

\mathbf{m}_{true} to equation (1), the solution can be alternatively and efficiently calculated through minimizing the following objective function

$$\mathcal{J}(\mathbf{m}) = \frac{1}{2} \|\mathbf{d}_{obs} - \mathbf{Fm}\|^2 \quad (5)$$

which evaluates the misfit between observed data \mathbf{d}_{obs} and the predicted data \mathbf{Fm} . Then the Hessian matrix (the second-order partial derivatives) of \mathcal{J} is denoted as⁶⁶

$$\mathbf{H} = \mathbf{F}^T \mathbf{F} \quad (6)$$

this quantity also contains the multi-actuation stacking process and is used for iteratively seeking the solution in the model space using a conjugate gradient (CG) method. For more details on the CG method, please refer to He et al.,⁶⁹ where the detailed implementation of the data residual, model residual, and predicted reflectivity model is described.

The schematic diagram of the LSRTM is shown in Figure 1, where the top part is the same as the conventional RTM. The stacking process was identified from implementations of multiple actuators. The initial model in this research for \mathbf{m} is zero-valued across the entire domain by assuming no damage in the background model to cause scattering. As a result, the first iteration of LSRTM becomes a product between an image from conventional RTM and a scaling factor (the step length calculated from CG). Also, taking the derivative of \mathbf{m} for equation (5) will generate $\mathbf{F}^T[\mathbf{d}_{obs} - \mathbf{Fm}]$. If \mathbf{m} is initially zero, $\mathbf{F}^T \mathbf{d}_{obs}$ becomes the same as conventional RTM represented in equation (2). For each iteration, the main computational costs come from the calculation of the forward and adjoint wavefields.

Numerical simulation

This section compares the RTM and LSRTM damage imaging results using ultrasonic guided waves. A finite difference algorithm was employed to simulate the flexural wave propagation based on the Mindlin plate theory. Only A_0 mode Lamb waves existed in the simulation. Details about the finite difference algorithm can be found in He and Yuan.⁵⁷ The plate was modeled with aluminum 6061-T6 with dimensions of 401 mm × 401 mm and a thickness of 2.28 mm (Figure 2). In the finite difference algorithm, the plate domain was discretized by a 401 × 401 mesh, with a 1 mm × 1 mm grid size. The material properties were assigned to every grid in the finite difference algorithm. In this section, all damage sites were modeled using Born approximation.

Since all the material properties and geometrical information are known a priori, the finite difference algorithm inputs the excitation as time-dependent pressure distributed over the nodes representing the actuator to generate the forward wavefield. A 2.5-cycle Hanning-windowed tone-burst excitation signal was applied to the actuator as an out-of-plane force. In all case studies shown in this article, the center frequency is set to 100 kHz, corresponding to a wavelength of 13.7 mm for the A_0 mode Lamb waves. The pixel size in the images is the same as the distance between two mesh points, which is smaller than 1/10 of the wavelength. The sensors were modeled as the grid points at their corresponding locations along with recording the out-of-plane velocities.

Rectangular damage

The first case in this section aims to provide a simple LSRTM application example. The next section focuses on a comparative base for the experimental results. Figure 2 shows the circular array used in this section, with a radius of 100 mm, consisting of 9 actuators and 36 sensors. These sensors record the simulated, out-of-plane velocity on the surface of the plate, which could be measured using a laser Doppler vibrometer (LDV) in experiments. Since the computational cost of the adjoint wavefield calculation does not increase along with the number of sensors increases, for LSRTM, more sensors and less actuators are preferred. Thus, the number of actuators is much less than that of the number of sensors (Figure 2). To understand the relationship between the number of actuators/sensors and the imaging quality, theoretical frameworks were derived for related imaging methods in Rose et al.⁵⁶ The selection of the number of actuators/sensors in our article aims to reflect the performance improvement of the least-squares engine when the number of actuators/sensors is relatively small, which can be limited by engineering requirements in SHM.

In this simulation case, a damage site, with a rectangular shape of 23 mm in length and 10 mm in width, was modeled as a constant scattering value based on Born approximation. The scattering value of the damage site is set to 0.5 with the center of the damage being set at the center of the plate, as shown in Figure 3(a).

The conventional RTM image using an NZLCC imaging condition is shown in Figure 3(b). However, the damage boundary is blurry, and the array shows artifacts with large values. In previous research,^{53,54} the time-reversed, damage-scattered signals were imposed at the sensor locations as boundary conditions during back-propagation such that the amplitude of the backward wavefield estimates the amplitude of the reflected

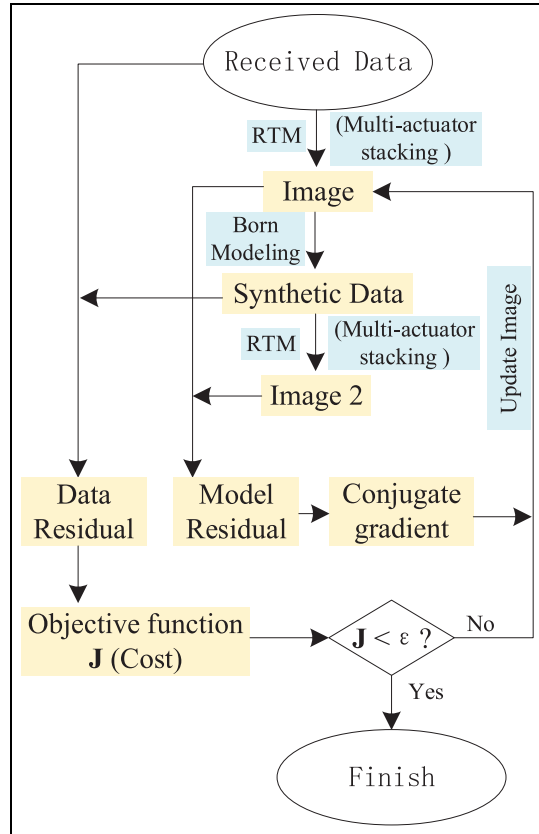


Figure 1. Schematic diagram of LSRTM.

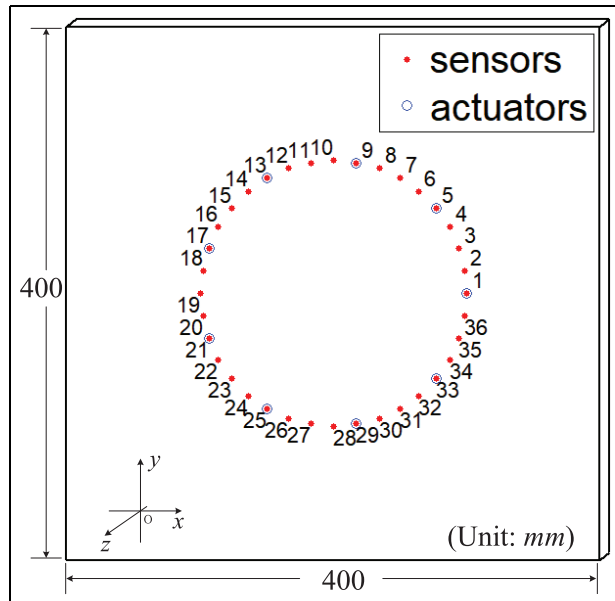


Figure 2. Illustration of the plate and the data acquisition circular array with numbering.

wavefield. The back-propagation implemented as such is less sensitive to the number of sensors.

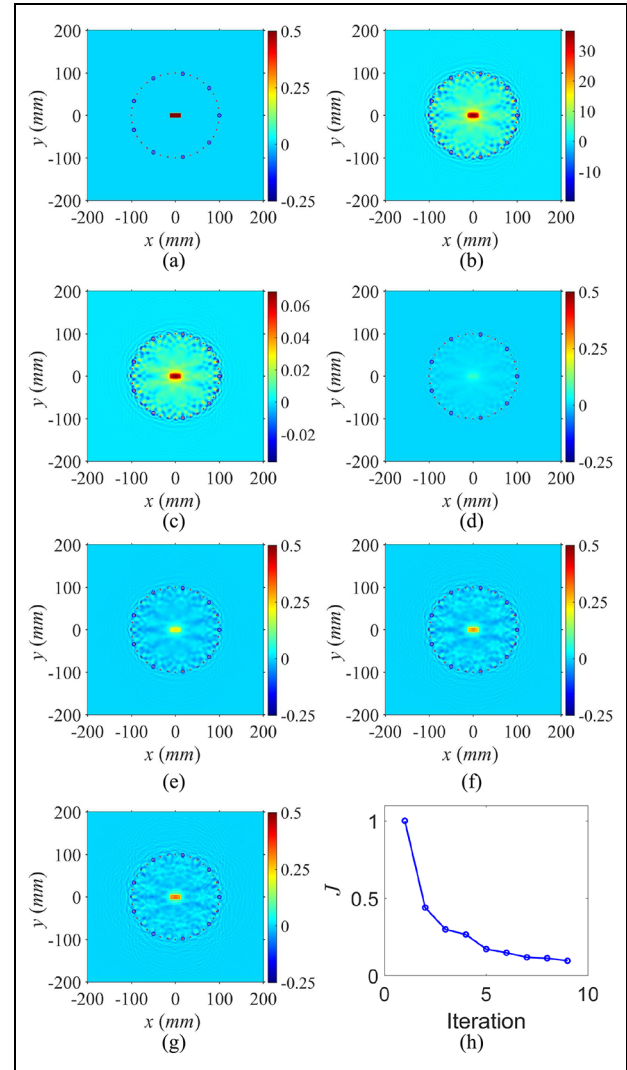


Figure 3. Numerical results for a rectangular damage: (a) Born model of the damage, (b) conventional RTM image (auto-scaled), (c) LSRTM image from the first iteration (auto-scaled), (d) to (g) LSRTM images (fix-scaled) from the first, third, sixth, and ninth iterations, and (h) the normalized objective function from LSRTM for the first nine iterations.

However, in order to calculate the adjoint wavefields in this research, the time-reversed, damage-scattered signals were used as source terms in back-propagation. More sensors lead to more input energy in the backward wavefield for conventional RTM, resulting in images with larger values. Thus, the maximum value is much larger than that in the original model in Figure 3(b). Damage images obtained this way do not provide useful information regarding the damage scattering amplitudes for conventional RTM.

The damage image from the first iteration of LSRTM is shown in Figure 3(c). Both Figure 3(b) and (c) are bounded by their particular maximum and

minimum values. The two images are nearly identical except that the latter automatically corrects the image amplitude during the forward modeling of LSRTM, thereby becoming advantageous for damage severity quantification. Since this pattern is seen throughout the entire research, conventional RTM image and the first iteration of LSRTM image will not be displayed together to reduce clutter.

The LSRTM results at iterations 1, 3, 6, and 9 are displayed with the same scale, as shown in Figure 3(d) to (g). Subsequently, as the iterations proceed, the artifacts within the array become weaker. The shape of the rectangular damage is clearer, with an increasing amplitude toward the true damage scattering amplitude of 0.5. The damage shape is illuminated considerably better. It has an amplitude of 0.351 of the damaged region, where the maximum damage scattering amplitude extracted from the first iteration is 0.065. LSRTM can automatically scale the predicted damage map to a meaningful range based on Born modeling, whereas conventional RTM images do not contain useful information regarding the absolute damage scattering amplitude, when back-propagation is implemented with source inputs.

In Figure 3(h), the normalized objective function \mathcal{J} (equation (5)) is monotonically decreasing. This behavior validates the correctness of the numerical simulation process. Since Born approximation was used such that the formulated modeling was linear, the objective function \mathcal{J} was expected to be convex. Therefore, it approaches the global minimum in a monotonically decreasing manner. The corresponding solutions (images) are least-squares estimates of the damage model. As previously shown in He et al.,⁶⁹ when using a limited-aperture array in guided wave application, artifacts exist around the damaged regions. However, those artifacts can also be effectively reduced over iterations in LSRTM.

Since the reflectivity is a constant positive value (0.5) in this case, the original model and the ninth LSRTM damage image are better presented only through the nonnegative values in the images as shown in Figure 4(a) and (b). For consistency, blue color will be set to represent zero for all of the damage images thereafter as in this figure. The iterative updates in LSRTM sharpen the damage shapes in addition to helping approaching the true damage scattering amplitude in the Born approximation.

A complex-shaped damage site

The second example studies a damage site of a complex shape with varying reflectivity, as shown in Figure 5(a). For example, pitting corrosion often has various scattering amplitudes over an irregular shape due to the

changes in thickness.⁷⁶ Only six actuators were used, as indicated in Figure 5(b).

In Figure 5(b), the conventional RTM image displays some degree of damage sizing but the damage shape is not clearly illuminated. The detailed damage features (e.g. the large amplitude locations, the “ring-shaped region” in Figure 5(a)) cannot be spotted. The ninth iteration of LSRTM imaging results are shown in Figure 5(c), the main shape of the damage model is displayed, and the orientation of the damage image matches the original model. The damaged region is illuminated with details such as the “ring-shaped region” and the “small hole” close to the center of the damage model. As stated previously, the objective function is monotonically decreasing (Figure 5(d)).

Multiple damage sites

In order to test the imaging capabilities of multiple, off-center, varying-sized, damage sites, another case (Figure 6(a)) was studied numerically. The six squared damage sites have side lengths (mm) of 8, 10, 12, 14, 16, and 18, respectively. All damage sites have a constant scattering amplitude of 1 with Born approximation. Only six actuators were used as indicated in Figure 6(b).

In Figure 6(b), the conventional RTM image estimates the damage locations but fails to quantify the shapes of the damage sites with relatively large artifacts. The 15th iteration LSRTM image is shown in Figure 6(c), where the damage locations and shapes significantly improved over conventional RTM. The distortion of the damage shapes, except for the smallest one, is limited with the consideration that only six actuators were used. The objective function is monotonically decreasing (Figure 6(d)), which shows the same patterns as in the previous examples. In Born approximation-based simulations for LSRTM imaging, when using the damage-scattered signals, this linear optimization behavior can always be observed.

Experimental results

The experimental setup is shown in Figure 7, for guided wave tomography in an aluminum alloy 6013-T6 plate. The system consisted of a function generator (Tek AFG3000), a power amplifier (Krohn-Hite 7602), an LDV (Polytec OFV-505), and a 2D translational stage (IAI ROBO). A laser beam pointed perpendicularly at the plate that measures the out-of-plane velocity. The aluminum plate had dimensions of 400 mm \times 400 mm \times 2.29 mm. A half-thickness notch with dimensions of 23 mm \times 10 mm was cut as a damage site. The actuators and the notch were on the same side of the plate while the LDV was scanned the other side with the

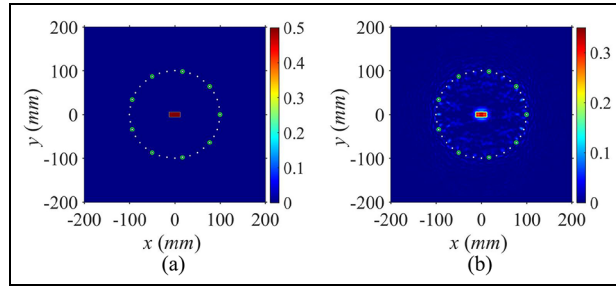


Figure 4. Numerical results for a rectangular damage by only showing positive values: (a) Born model of the complex-shaped damage, and (b) LSRTM images from the ninth iteration (the same input as in Figure 3(g)).

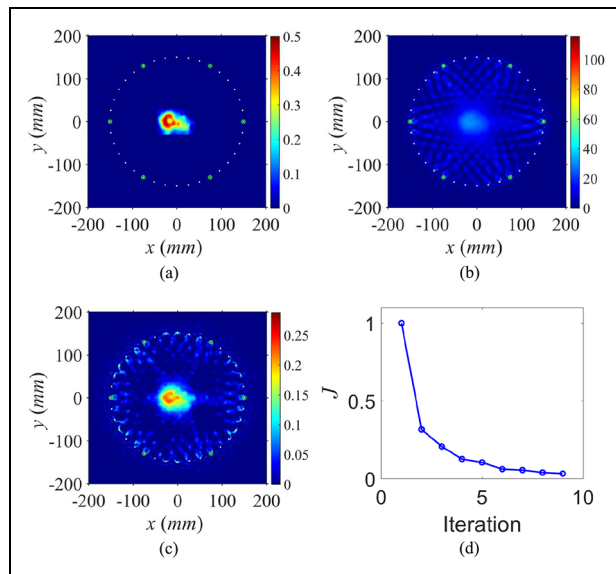


Figure 5. Numerical results for a complex-shaped damage: (a) Born model of the complex-shaped damage, (b) Conventional RTM image, (c) LSRTM image from the ninth iteration, and (d) the normalized objective function from LSRTM for the first nine iterations.

same numbering in Figure 2. The total time for inversion is 160 μ s.

Experimental and simulated signal comparison

To verify the accuracy of the wave propagation simulator implemented in this research, the experimentally acquired signals were compared with the simulated signals. The theory of LSRTM, as introduced in the “Theoretical formulation of LSRTM” section, is based on Born approximation, which cannot always be strictly satisfied in engineering applications. In order to examine the influence of the discrepancies caused by the errors of Born modeling, another numerical

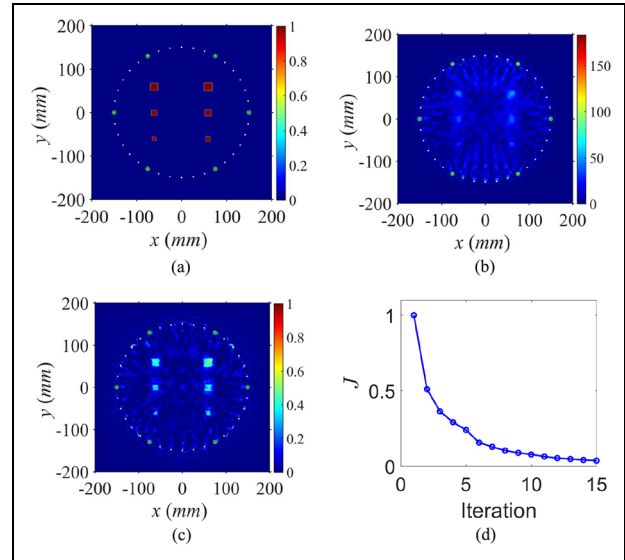


Figure 6. Numerical results for six square-shaped damage sites using an excitation signal with a center frequency of 100 kHz: (a) Born model of the six damage sites, (b) conventional RTM image, (c) LSRTM images from the 15th iteration, and (d) the objective function from LSRTM for the first 15 iterations.

method was implemented to generate damage-scattered signals, which was modeled by changing the parameters in the flexural wave equations for damage regions as explained in He and Yuan.⁵⁷ This scattering modeling method will be referred to as “non-Born” modeling/scattering in this article. The non-Born modeling in the following simulations for this work was to change the parameter of the thickness in the flexural wave equations.

The signals excited from actuator 1 and then received by the 36 sensors from both the Born and the non-Born modeling simulation and from the experiment are compared side-by-side in Figure 8. Since the sensing array is circular, an “arc”-shaped event (direct arrivals) can be spotted from all of the three cases.

In the Born scattering case (Figure 8(a)), since the scattering amplitude was set to 0.5, damage-scattered waves were large enough to be seen at the “tip of the arc event,” even when shown together with the direct arrivals. The amplitude of the scattered waves in Figure 8(b) and (c) is much smaller than that in Figure 8(a). Each of the previous simulations used absorbing boundary condition, while the experiments had reflections of the plate boundaries, which can be seen later in Figure 8(c).

Inversion of the total signals

The next section introduces an experiment where the damaged plate was the initial structure for inspection in

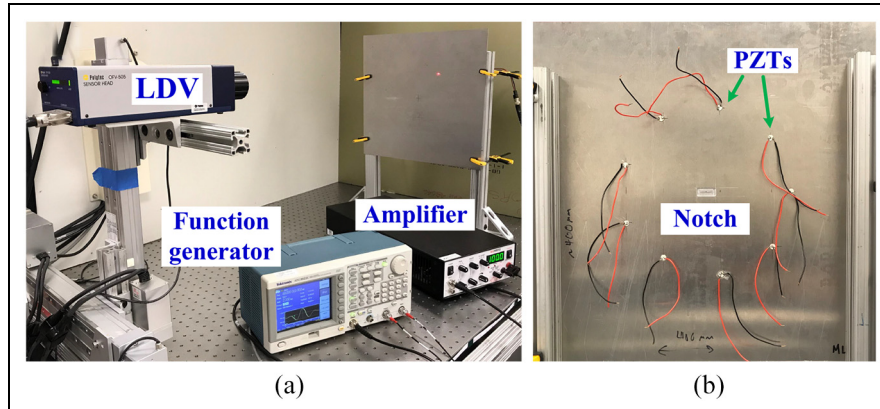


Figure 7. (a) Experimental setup for the LSRTM tomography and (b) the backside of the plate.

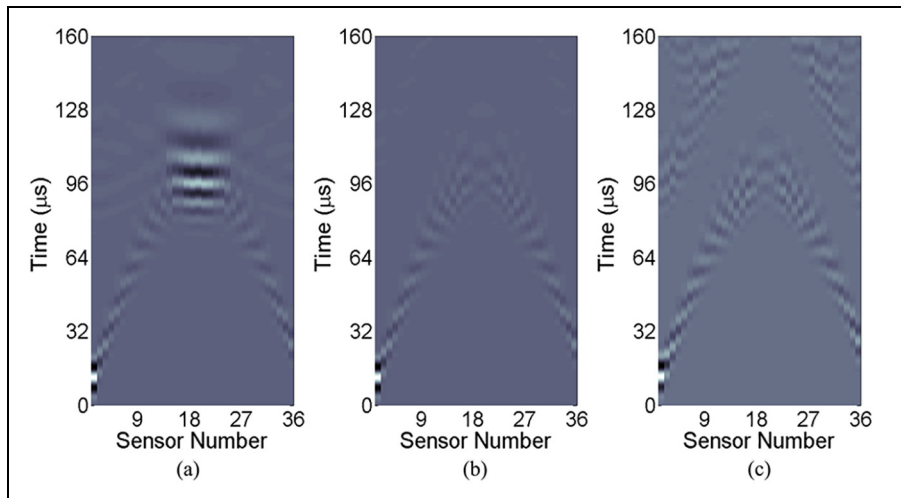


Figure 8. Signals received by the 36 sensors, excited by actuator I in (a) Born modeling simulation, (b) non-Born modeling simulation, and (c) experimental measurements.

a manner that suggests the baseline signals for the pristine plate as unavailable. It resembles NDE scenarios, where baseline measurements generally do not exist. In some complex structures, baseline-subtraction-free methods can be used to extract the damage-scattered signal.⁷⁷ However, it would still be more convenient if the baseline signals are not needed for imaging. Since only a single source was used in each excitation while the damage-scattered signals existed for all of the excitations, inversions might be possible using all of the received signals. Those signals contain direct arrivals from the actuator, damage-scattered signals, and perhaps even plate boundary reflections, which will be referred to as the “total signals.”

In order to explore the possibility of inversion using the total signals, comparative cases were simulated with Born approximation and inverted using damage-scattered signals and total signals, respectively. It is

important to note that in total signals from simulations, since absorbing boundary conditions were used, only direct arrivals and the damage-scattered signals exist.

The damage image at the first iteration using LSRTM is shown in Figure 9 with the same arrangement of actuators and sensors as in Figure 4, where array locations are not shown to observe the imaging results at the array locations. The damage image at the first iteration using damage-scattered signals (Figure 9(a)) is similar to that of using total signals (Figure 9(b)), since they are blurry and have relatively large artifacts outside of the rectangular damaged region.

At the ninth iteration using LSRTM, both results using damage-scattered signals (Figure 9(c)) and using total signals (Figure 9(d)) show sharpened damage regions and suppressed artifacts. The scattering amplitude of the damaged region in both images is

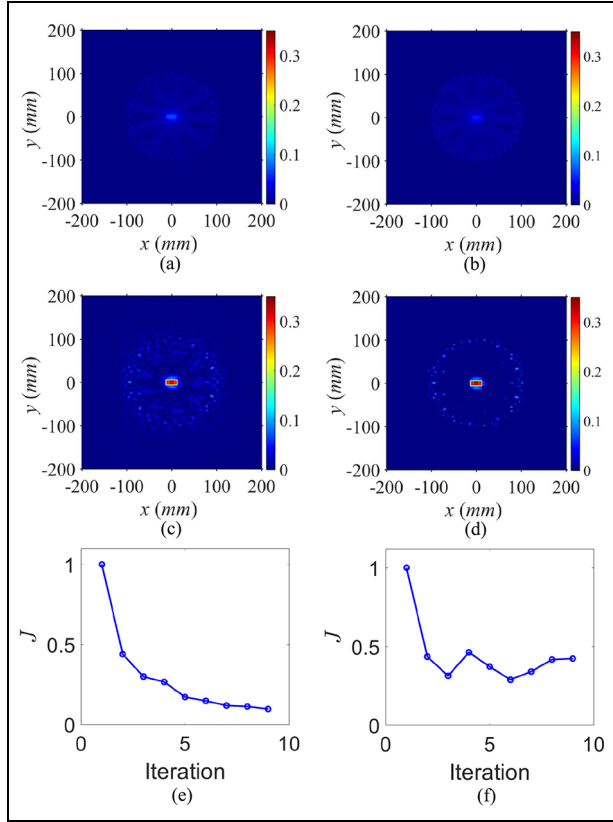


Figure 9. Images comparison from damage-scattered signals and total received signals using Born modeling. Conventional RTM images using (a) damage-scattered signals and (b) total received signals; ninth iteration of LSRTM images using (c) damage-scattered signals and (d) total received signals; normalized objective functions using (e) damage-scattered signals and (f) total received signals.

approaching 0.35. Figure 9(d) displays even less artifacts within the circular array compared to Figure 9(c), which is possible because the gradient in the total signal inversion needed to focus more on fitting the scattering map at the source/array locations such that it reduced the artifacts within the array. The objective function in the total signal inversion (Figure 9(f)) does not decrease monotonically as in the damage scattering inversion (Figure 9(e)) is likely due to the aforementioned reason as well. To summarize, the inversion with the direct arrivals did not degrade the performance in comparison to that when only using damage-scattered signals with Born modeling.

Experimental results using LSRTM

Compared to the experimental results, signals generated by the aforementioned “non-Born” modeling with

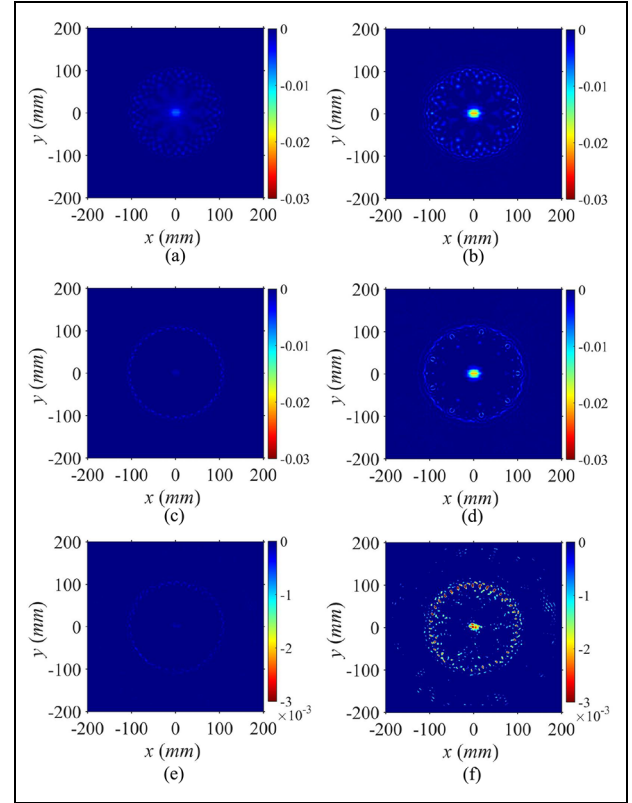


Figure 10. The first iteration of LSRTM images using (a) damage-scattered signals from non-Born modeling, (c) total received signals from non-Born modeling, (e) total experimental signals; the 3rd iteration of LSRTM images using (b) damage-scattered signals from non-Born modeling, (d) total received signals from non-Born modeling, and (f) total experimental signals.

the plate thickness changed to 1.14 mm (half-thickness) were used for inversion. The array setup and damage shape were implemented exactly like Figure 3 for Born modeling, where images from the first and third iterations can be used for comparison in this section. To be comparable with the to-be-introduced experimental results, the images of the first and third iteration of LSRTM using damage-scattered signals with “non-Born” modeling are shown in Figure 10(a) and (b), respectively. Similar to the Born modeling results in Figure 9(c), the third iteration is much better focused on the damage location, thereby suppressing the artifacts within the circular array. Although the damage sizing with “non-Born” modeling is relatively accurate, the shape displayed in Figure 10(b) shows wider and more blurry damage boundaries as compared to the original damage model. The damaged region in Figure 10(b) has negative values and smaller amplitudes in comparison with Figure 9(c), since the amplitude of the

damage-scattered signals using Born modeling (with a value of 0.5) is much larger than those of using non-Born modeling (half-thickness for parameter changes in wave equations).

The total signal inversion with the “non-Born” modeling at the first and third iterations is shown in Figure 10(c) and (d). The artifacts for the first iteration (Figure 10(c)) are already suppressed, compared to Figure 10(a). The damaged region from the third iteration (Figure 10(d)) is imaged with a larger amplitude and clearer shape compared with the first iteration (Figure 10(c)). Compared to the third iteration of using only the damage-scattered signals (Figure 10(b)), the total signal inversion of the third iteration (Figure 10(d)) shows similar results for the damaged region with larger artifacts at the source locations but less artifacts within the array. With regard to the circular array setup used in this research, the damage imaging is not worsened by the lack of baseline signals. The artifact suppression within the circular using total signals is arguably improved over the implementation of using the pure damage-scattered signals, which can be hard to obtain for engineering applications.

Finally, the first and third iterations of LSRTM inversion using the experimentally measured total signals are shown in Figure 10(e) and (f), respectively. The previously mentioned boundary reflections in experiments caused widespread but low-amplitude artifacts. In order to suppress those artifacts, a 10% threshold of its maximum value was applied to both Figure 10(e) and (f).

The first iteration of experimental inversion (Figure 10(e)) and the first iteration results using total non-Born signals in simulation (Figure 10(c)) are very similar, where only the array and the damaged region can be observed. As the inversion progresses to the third iteration, Figure 10(f) shows the damage location and approximate sizing. However, the shape of the original rectangular damage is not well-displayed. This could be due to the alignment errors between the experimental data acquisition and the simulated locations for inversion. The small errors in actuator and sensor locations for inversion and the relative positioning errors between the array and the damage have possibly caused the irregular shape of the damaged region in Figure 10(f). For the same reason, the artifacts at the LDV scanning points are very large and lead to over-fitting, and thus, only iterations up to the third one are shown for comparison.

Better alignment can be achieved to align the LDV scanning points (e.g. with a smaller radius of the circular array) on the same side of the plate with the notch and the actuators for these current testing systems. However, those alignment errors should be minimized when using a commercial transducer array. Therefore,

perfecting the array locations during inversion was not pursued in this research. Another reason that the imaged damage shape is not a perfect rectangle in that the experiment states that Born approximation is not strictly respected in experiments.

Conclusion

LSRTM is proposed and evaluated with a circular array for damage imaging using guided wave tomography. The forward and adjoint operators are defined for this NDT/SHM scenario, followed by a CG method being implemented to optimize the damage model prediction. Based on Born approximation, quantitative inversion results using damage-scattered signals are shown through numerical case studies of a rectangular damage site, a complex-shaped damage site, and multiple, varying-sized damage sites, respectively. The proposed LSRTM allows for improved shape reconstructions and reduced artifacts with the same number of sensors over conventional RTM. In addition, it enables the damage modeling capability within Born approximation. In order to reduce the computational cost, the proposed setup uses a small number of actuators with a relatively large number of sensors, based on the fact that the computational cost of forward and adjoint calculation is only sensitive to the number of actuators but not the sensors.

The effects with or without the direct arrivals from the actuators to inversion were also numerically studied through both born modeling and changing the material properties in wave equations (referred to as non-Born modeling in this article). The results show that the influence of direct arrivals is negligible because the actuator locations are spatially focused, which enables another positive feature of LSRTM.

Finally, experiments were performed using piezoelectric wafers as actuators and LDV to receive the signals at an array of locations as sensors. With small errors in alignments, the damage images using experimental data and those using numerically generated data show consistency. The potential applicability of LSRTM as a viable NDT/SHM technique is verified, aiming for the application as part of a digital twin environment for damage modeling and tracking. The proposed framework not only utilize the scattering effects for accurate imaging but also endorses the possibility of dealing with structural complexity if more advanced numerical solvers are used.

Declaration of conflicting interests

The author(s) declared no potential conflicts of interest with respect to the research, authorship, and/or publication of this article.

Funding

The author(s) disclosed receipt of the following financial support for the research, authorship, and/or publication of this article: This study was supported by NASA's Convergent Aeronautics Solutions: Digital Twin project (#NNL09AA00A).

ORCID iD

Jiaze He  <https://orcid.org/0000-0001-6198-0688>

References

1. Cawley P. Structural health monitoring: closing the gap between research and industrial deployment. *Struct Health Monit* 2018; 17: 1225–1244.
2. Doherty C and Chiu W. Scattering of ultrasonic-guided waves for health monitoring of fuel weep holes. *Struct Health Monit* 2012; 11(1): 27–42.
3. Yuan FG. *Structural health monitoring (SHM) in aerospace structures*. Cambridge: Woodhead Publishing, 2016.
4. Liu Z, Yu H, Fan J, et al. Baseline-free delamination inspection in composite plates by synthesizing non-contact air-coupled Lamb wave scan method and virtual time reversal algorithm. *Smart Mater Struct* 2015; 24(4): 045014.
5. Harb M and Yuan F. Barely visible impact damage imaging using non-contact air-coupled transducer/laser Doppler vibrometer system. *Struct Health Monit* 2016; 16: 663–673.
6. Bhuiyan MY and Giurgiutiu V. Multiphysics simulation of low-amplitude acoustic wave detection by piezoelectric wafer active sensors validated by in-situ AE-fatigue experiment. *Materials* 2017; 10(8): 962.
7. Zhou W, Li H and Yuan FG. An anisotropic ultrasonic transducer for Lamb wave applications. *Smart Struct Syst* 2016; 17(6): 1055–1065.
8. Ren B and Lissenden CJ. PVDF multielement Lamb wave sensor for structural health monitoring. *IEEE T Ultrason Ferr* 2016; 63(1): 178–185.
9. Park B, Sohn H, Malinowski P, et al. Delamination localization in wind turbine blades based on adaptive time-of-flight analysis of noncontact laser ultrasonic signals. *Non-destruct Test Eva* 2017; 32(1): 1–20.
10. Mal A, Ricci F, Banerjee S, et al. A conceptual structural health monitoring system based on vibration and wave propagation. *Struct Health Monit* 2005; 4(3): 283–293.
11. Shen Y. *Structural health monitoring using linear and non-linear ultrasonic guided waves*. Doctoral dissertation, 2014, <https://scholarcommons.sc.edu/cgi/viewcontent.cgi?referer=https://scholar.google.co.in/&httpsredir=1&article=3902&context=etd>
12. Ihn JB and Chang FK. Detection and monitoring of hidden fatigue crack growth using a built-in piezoelectric sensor/actuator network: II. Validation using riveted joints and repair patches. *Smart Mater Struct* 2004; 13(3): 621.
13. Sohn H, Park HW, Law KH, et al. Damage detection in composite plates by using an enhanced time reversal method. *J Aerospace Eng* 2007; 20(3): 141–151.
14. Wilcox PD and Zhang J. Quantification of the effect of array element pitch on imaging performance. *IEEE T Ultrason Ferr* 2018; 65(4): 600–616.
15. Hunter AJ, Drinkwater BW and Wilcox PD. The wave-number algorithm for full-matrix imaging using an ultrasonic array. *IEEE T Ultrason Ferr* 2008; 55(11): 2450–2462.
16. Budyn N, Bevan R, Croxford AJ, et al. Sensitivity images for multi-view ultrasonic array inspection. *AIP Conf Proc* 2018; 1949: 080001.
17. Michaels JE. Detection, localization and characterization of damage in plates with an in situ array of spatially distributed ultrasonic sensors. *Smart Mater Struct* 2008; 17(3): 035035.
18. Yu L and Giurgiutiu V. In situ 2-D piezoelectric wafer active sensors arrays for guided wave damage detection. *Ultrasonics* 2008; 48(2): 117–134.
19. Ambroziński Ł, Stepinski T and Uhl T. Efficient tool for designing 2D phased arrays in Lamb waves imaging of isotropic structures. *J Intel Mat Syst Str* 2015; 26(17): 2283–2294.
20. Kerbrat E, Ing R, Prada C, et al. The D.O.R.T. method applied to detection and imaging in plates using lamb waves. *AIP Conf Proc* 2001; 557: 934–940.
21. He J and Yuan FG. Lamb wave-based subwavelength damage imaging using the DORT-MUSIC technique in metallic plates. *Struct Health Monit* 2016; 15(1): 65–80.
22. Friswell MI. Damage identification using inverse methods. In: Morassi A and Vestroni F (eds) *Dynamic methods for damage detection in structures*. Vienna: Springer, 2008, pp. 13–66.
23. Inman DJ, Farrar CR, Junior VL, et al. *Damage prognosis: for aerospace, civil and mechanical systems*. Hoboken, NJ: John Wiley & Sons, 2005.
24. Hu B, Hu N, Li L, et al. Tomographic reconstruction of damage images in hollow cylinders using lamb waves. *Ultrasonics* 2014; 54(7): 2015–2023.
25. Liu Y, Zhou S, Ning H, et al. An inverse approach of damage identification using lamb wave tomography. *Sensors* 2019; 19(9): 2180.
26. Koreck J, Valle C, Qu J, et al. Computational characterization of adhesive layer properties using guided waves in bonded plates. *J Nondestruct Eval* 2007; 26(2–4): 97–105.
27. Zhao J, Qiu J and Ji H. Reconstruction of the nine stiffness coefficients of composites using a laser generation based imaging method. *Compos Sci Technol* 2016; 126: 27–34.
28. Hudson TB and Yuan FG. Automated in-process cure monitoring of composite laminates using a guided wave-based system with high-temperature piezoelectric transducers. *J Nondestruct Eval Diagn Progn Eng Syst* 2018; 1(2): 021008.
29. Carcreff E, Laroche N, Braconnier D, et al. Improvement of the total focusing method using an inverse problem approach. In: *Proceedings of the 2017 IEEE international*

- ultrasonics symposium (IUS)*, Washington, DC, 6–9 September 2017, pp. 1–4. New York: IEEE.
30. Leonard KR, Malyarenko EV and Hinders MK. Ultrasonic Lamb wave tomography. *Inverse Probl* 2002; 18(6): 1795.
 31. Volker A and Bloom J. Experimental results of guided wave travel time tomography. *AIP Conf Proc* 2011; 1335: 215–222.
 32. Devaney AJ. *Mathematical foundations of imaging, tomography and wavefield inversion*. Cambridge: Cambridge University Press, 2012.
 33. Belanger P, Cawley P and Simonetti F. Guided wave diffraction tomography within the Born approximation. *IEEE T Ultrason Ferr* 2010; 57(6): 1405–1418.
 34. Chan E, Rose LF and Wang CH. An extended diffraction tomography method for quantifying structural damage using numerical Green's functions. *Ultrasonics* 2015; 59: 1–13.
 35. Huthwaite P and Simonetti F. High-resolution guided wave tomography. *Wave Motion* 2013; 50(5): 979–993.
 36. Huthwaite P. Guided wave tomography with an improved scattering model. *P R Soc A* 2016; 472(2195): 20160643.
 37. Brigante M and Sumbatyan M. Application of the inverse diffraction technique to the problem of reconstruction of complexly shaped flaws by ultrasonic methods. *Russ J Nondestruct Test* 2010; 46(2): 98–111.
 38. Devaney A. Inverse source and scattering problems in ultrasonics. *IEEE T Son Ultrason* 1983; 30(6): 355–364.
 39. Ogam E, Fellah ZA and Baki P. The inverse problem of acoustic wave scattering by an air-saturated poroelastic cylinder. *J Acoust Soc Am* 2013; 133(3): 1443–1457.
 40. Huthwaite P, Lowe M and Cawley P. Guided wave tomography performance analysis. *AIP Conf Proc* 2016; 1706: 020021.
 41. Rao J, Ratssepp M, Lisevych D, et al. On-line corrosion monitoring of plate structures based on guided wave tomography using piezoelectric sensors. *Sensors* 2017; 17(12): 2882.
 42. Rao J, Ratssepp M and Fan Z. Guided wave tomography based on full waveform inversion. *IEEE T Ultrason Ferr* 2016; 63(5): 737–745.
 43. Wertz J, Homa L, Welter J, et al. Case study of model-based inversion of the angle beam ultrasonic response from composite impact damage. *J Nondestruct Eval Diagn Progn Eng Syst* 2018; 1(4): 041001.
 44. Ma Y, Hale D, Gong B, et al. Image-guided sparse-model full waveform inversion. *Geophysics* 2012; 77(4): R189–R198.
 45. Chang Y, Zi Y, Zhao J, et al. An adaptive sparse deconvolution method for distinguishing the overlapping echoes of ultrasonic guided waves for pipeline crack inspection. *Meas Sci Technol* 2017; 28(3): 035002.
 46. Huthwaite P. Accelerated finite element elastodynamic simulations using the GPU. *J Comput Phys* 2014; 257: 687–707.
 47. Modrak RT, Borisov D, Lefebvre M, et al. SeisFlows—flexible waveform inversion software. *Comput Geosci* 2018; 115: 88–95.
 48. Volker A, van Zon T, Enthoven D, et al. 1D profiling using highly dispersive guided waves. *AIP Conf Proc* 2015; 1650: 754–760.
 49. Nishino H. An investigation of reflection coefficients of the T(0, 1) mode guided waves at axisymmetric defects and inverse problem analyses for estimations of defect shapes. *Mater Trans* 2015; 56(1): 120–128.
 50. Zhou W, Li H and Yuan FG. Fundamental understanding of wave generation and reception using d36 type piezoelectric transducers. *Ultrasonics* 2015; 57: 135–143.
 51. Zhou W, Yuan FG and Shi T. Guided torsional wave generation of a linear in-plane shear piezoelectric array in metallic pipes. *Ultrasonics* 2016; 65: 69–77.
 52. Wang B and Hirose S. Inverse problem for shape reconstruction of plate-thinning by guided SH-waves. *Mater Trans* 2012; 53(10): 1782–1789.
 53. He J and Yuan FG. Lamb-wave-based two-dimensional areal scan damage imaging using reverse-time migration with a normalized zero-lag cross-correlation imaging condition. *Struct Health Monit* 2016; 16: 444–457.
 54. He J and Yuan FG. A quantitative damage imaging technique based on enhanced CCRTM for composite plates using 2D scan. *Smart Mater Struct* 2016; 25(10): 105022.
 55. Baysal E, Kosloff DD and Sherwood JW. Reverse time migration. *Geophysics* 1983; 48(11): 1514–1524.
 56. Rose LF, Chan E and Wang CH. A comparison and extensions of algorithms for quantitative imaging of laminar damage in plates. I. Point spread functions and near field imaging. *Wave Motion* 2015; 58: 222–243.
 57. He J and Yuan FG. Damage identification for composite structures using a cross-correlation reverse-time migration technique. *Struct Health Monit* 2015; 14(6): 558–570.
 58. Yan J and Sava P. Isotropic angle-domain elastic reverse-time migration. *Geophysics* 2008; 73(6): S229–S239.
 59. Duan Y and Sava P. Scalar imaging condition for elastic reverse time migration. *Geophysics* 2015; 80(4): S127–S136.
 60. Rocha D, Sava P and Tanushev N. Acoustic wavefield imaging using the energy norm. In: *SEG technical program expanded abstracts 2015*, New Orleans, LA, 18–23 October 2015, pp. 4085–4090. Tulsa, OK: Society of Exploration Geophysicists.
 61. Rocha D, Tanushev N and Sava P. Isotropic elastic wavefield imaging using the energy norm. *Geophysics* 2016; 81(4): S207–S219.
 62. Rocha D, Tanushev N and Sava P. Anisotropic elastic wavefield imaging using the energy norm. *Geophysics* 2017; 82: S225–S234.
 63. Rao J, Ratssepp M and Fan Z. Limited-view ultrasonic guided wave tomography using an adaptive regularization method. *J Appl Phys* 2016; 120(19): 194902.
 64. Kuehl H and Sacchi M. Robust AVP estimation using least-squares wave-equation migration. In: *SEG technical program expanded abstracts 2002*, Salt Lake City, UT, 6–11 October 2002, pp. 281–284. Tulsa, OK: Society of Exploration Geophysicists.
 65. Dai W and Schuster GT. Plane-wave least-squares reverse-time migration. *Geophysics* 2013; 78(4): S165–S177.

66. Dong S, Cai J, Guo M, et al. Least-squares reverse time migration: towards true amplitude imaging and improving the resolution. In: *SEG technical program expanded abstracts 2012*, Las Vegas, NV, 4–9 November 2012, pp. 1–5. Tulsa, OK: Society of Exploration Geophysicists.
67. Rocha D and Sava P. Elastic least-squares reverse time migration using the energy norm. *Geophysics* 2018; 83(3): S237–S248.
68. Rocha D, Sava P and Guitton A. 3D acoustic least-squares reverse time migration using the energy norm. *Geophysics* 2018; 83(3): S261–S270.
69. He J, Rocha DC, Leser PE, et al. Least-squares reverse time migration (LSRTM) for damage imaging using Lamb waves. *Smart Mater Struct* 2019; 28(6): 065010.
70. Glaessgen E and Stargel D. The digital twin paradigm for future NASA and US Air Force vehicles. In: *Proceedings of the 53rd AIAA/ASME/ASCE/AHS/ASC structures, structural dynamics and materials conference 20th AIAA/ASME/AHS adaptive structures conference 14th AIAA*, Honolulu, HI, 23–26 April 2012, p. 1818. Reston, VA: AIAA.
71. He J, Leckey CA, Leser PE, et al. Multi-mode reverse time migration damage imaging using ultrasonic guided waves. *Ultrasonics* 2019; 94: 319–331, <http://www.science-direct.com/science/article/pii/S0041624X18303846>
72. Hudson J and Heritage J. The use of the born approximation in seismic scattering problems. *Geophys J Int* 1981; 66(1): 221–240.
73. Duan Y, Guitton A and Sava P. Elastic least-squares reverse time migration. *Geophysics* 2017; 82(4): S315–S325.
74. Claerbout JF. *Earth soundings analysis: processing versus inversion*, vol. 6. Oxford: Blackwell Scientific Publications, 1992.
75. Aoki N and Schuster GT. Fast least-squares migration with a deblurring filter. *Geophysics* 2009; 74(6): WCA83–WCA93.
76. Volker A, van Zon T and van der Leden E. Field trials results of guided wave tomography. *AIP Conf Proc* 2015; 1650: 615–621.
77. He J, Leser PE, Leser WP, et al. IWSHM 2017: damage-scattered wave extraction in an integral stiffened isotropic plate: a baseline-subtraction-free approach. *Struct Health Monit* 2018; 17: 1365–1376.